

UC Berkeley

UC Berkeley Previously Published Works

Title

Photoelectron spectroscopy of cryogenically cooled NiO 2 – via slow photoelectron velocity-map imaging

Permalink

<https://escholarship.org/uc/item/7qg9p3q1>

Journal

Physical Chemistry Chemical Physics, 24(29)

ISSN

1463-9076

Authors

Babin, Mark C

DeWitt, Martin

Lau, Jascha A

et al.

Publication Date

2022-07-27

DOI

10.1039/d2cp02396b

Copyright Information

This work is made available under the terms of a Creative Commons Attribution-NonCommercial License, available at <https://creativecommons.org/licenses/by-nc/4.0/>

Peer reviewed

Photoelectron spectrum of cryogenically cooled NiO_2^- *via* slow photoelectron velocity-map imaging

Mark C. Babin,^{†,a)} Martin DeWitt,[†] Jascha A. Lau,[†] Marissa L. Weichman,^{†,b)} Jongjin B. Kim,^{†,c)}
Lan Cheng,^{∇,*} Daniel M. Neumark^{†,⊥,*}

[†] Department of Chemistry, University of California, Berkeley, CA 94720, USA.

[∇] Department of Chemistry, Johns Hopkins University, Baltimore, Maryland 21218, USA.

[⊥] Chemical Sciences Division, Lawrence Berkeley National Laboratory, Berkeley, CA 94720, USA.

^{a)} Current address: Department of Chemistry and Chemical Biology, Harvard University, 12 Oxford St, Cambridge, MA 02138, USA.

^{b)} Current address: Department of Chemistry, Princeton University, Princeton, New Jersey 08544, USA

^{c)} Current address: KLA Corporation, 1 Technology Dr, Milpitas, CA 95035

Corresponding Authors

* lcheng24@jhu.edu, dneumark@berkeley.edu

Abstract:

High-resolution anion photoelectron spectra of cryogenically cooled NiO_2^- anions, obtained using slow photoelectron velocity-map imaging (cryo-SEVI), are presented in tandem with coupled cluster electronic structure calculations including relativistic effects. The experimental spectra encompass the $\tilde{X}^1 \Sigma_g^+ \leftarrow \tilde{X}^2 \Pi_g$, $\tilde{a}^3 \Pi_g \leftarrow \tilde{X}^2 \Pi_g$, and $\tilde{A}^1 \Pi_g \leftarrow \tilde{X}^2 \Pi_g$ photodetachment transitions of linear $\text{ONiO}^{0/-}$, revealing previously unobserved vibrational structure in all three electronic bands. The high-resolution afforded by cryo-SEVI allows for the extraction of vibrational frequencies for each state, congruent with those previously measured in the ground state and in good agreement with scalar-relativistic coupled-cluster calculations. Previously unobserved vibrational structure is observed in the $\tilde{a}^3 \Pi_g$ and $\tilde{A}^1 \Pi_g$ states and is tentatively assigned. Further, a refined electron affinity of 3.0464(7) eV for NiO_2 is obtained as well as precise term energies for the \tilde{a} and \tilde{A} states of NiO_2 of 0.3982(7) and 0.7422(10) eV, respectively. Numerous Franck-Condon forbidden transitions involving the doubly degenerate ν_2 bending mode are observed and ascribed to Herzberg-Teller coupling to an excited electronic state.

I. Introduction:

Nickel oxides are an important class of catalytic materials with a wide range of industrial applications including the formation of syngas,^{1,2} oxidative dehydrogenation of alkanes,^{3,4} and carbon monoxide oxidation.⁵ Therefore, understanding their properties is of both technological and fundamental importance. While much of the emphasis of nickel oxide catalysis involves condensed phase experiments, the gas phase study of isolated mass-selected metal oxide clusters provides a complementary molecular-level understanding of the structure and reactivity of these species.^{6,7} Here, we report high-resolution anion photoelectron spectra of cryogenically cooled NiO_2^- , revealing a wealth of vibronic structure throughout the three lowest-lying electronic states of NiO_2 .

There are relatively few experimental studies concerning the structure⁸⁻¹² and reactivity of $\text{NiO}_2^{0/-}$.¹³⁻¹⁶ Neutral NiO_2 was first studied in ideal gas matrices, where three isomers were identified in an Ar matrix:⁹ cyclic $\text{Ni}(\text{O}_2)$, bent NiOO , and linear ONiO (referred to as NiO_2 hereafter). Subsequent work in Ne matrices found preferential formation of the linear NiO_2 species with trace $\text{Ni}(\text{O}_2)$, allowing for the extraction of two and three vibrational frequencies for these species, respectively.¹² In the gas phase, anion photoelectron spectroscopy (PES) has been used to probe the geometric and electronic structure of these species. The first PES study of NiO_2^- was performed by Wu and coworkers,¹⁰ who observed photodetachment from both the bent $\text{Ni}(\text{O}_2)$ and linear NiO_2 anions, finding the electron affinity (EA) of $\text{Ni}(\text{O}_2)$ to be 0.82(3) eV, considerably lower than that of NiO_2 at 3.05(1) eV. The NiO_2 band showed partially resolved vibrational structure with a frequency of 750 cm^{-1} . This work also found transitions to two low-lying electronic states of NiO_2 with term energies of 0.40(2) and 0.77(3) eV. Subsequent anion PES work performed by Ramond *et al.*¹¹ reexamined the ground state spectrum of NiO_2 with improved resolution, yielding a refined EA of 3.043(5) eV as well as the ν_1 symmetric stretch frequency of 745(30) cm^{-1} from a progression in this mode.

The electronic and vibrational structure of NiO_2 pose a considerable challenge to theory owing to its multireference nature.^{17,18} Treatments using density functional theory,^{9,12,19-21} coupled cluster methods,²¹ and multireference methods²² have found a ${}^1\Sigma_g^+$ ground electronic term for linear

NiO₂ that lies 0.7-1.5 eV below the Ni(O₂) structure. In both structures, there are numerous low-lying singlet and triplet species calculated to reside within ~2 eV of the ground state. The most definitive of these works is a joint multiconfiguration self-consistent field (MCSCF) and multireference configuration interaction (MRCI) study by Hübner,²² which finds a $^1\Sigma_g^+$ ground state with $^3\Pi_g$ and $^1\Pi_g$ states lying 0.537 and 0.943 eV higher in energy, in good agreement with the observed term energies from anion PES. Less work has been done on the NiO₂⁻ anion, with an early DFT study by Gustev *et al.*²⁰ finding a 2A_2 bent ground state and more recent DFT work by Deng and coworkers¹⁹ finding a linear $^2\Pi_g$ ground state.

Here, we utilize slow electron velocity-map imaging spectroscopy of cryogenically-cooled anions (cryo-SEVI), a high-resolution variant of anion photoelectron spectroscopy, to study the photodetachment of NiO₂⁻. In this method, cold ions are detached with a tunable laser and the resultant electron kinetic energy distribution is analyzed by a velocity-map imaging (VMI) spectrometer that is optimized for the detection of slow electrons, yielding photoelectron spectra with sub-meV resolution.^{23,24} Revisiting the photoelectron spectra of NiO₂⁻ with cryo-SEVI provides substantial improvements in resolution over previous work. Beyond well-resolved vibrational structure in the ground and excited states, we observe a number of FC-forbidden transitions in the ground state that display behavior distinct from that of the FC-allowed transitions near the photodetachment threshold. These features are ascribed to vibronic coupling to an excited electronic state. Our findings are supported by scalar-relativistic coupled-cluster calculations, with computed term energies and vibrational frequencies in good agreement with our observed spectra.

II. Experimental Methods:

The cryo-SEVI method has been described in detail previously.^{23,25,26} Here, NiO₂⁻ anions are formed *via* laser ablation using a rotating and translating nickel disk onto which a frequency-doubled Nd:YAG is focused. The resulting plasma is entrained within a pulse of He carrier gas from an Even-Lavie solenoid valve,²⁷ with residual O₂ in this carrier gas serving to form NiO₂⁻

as it passes through a narrow channel to foster collisional cooling and cluster formation. The ions then pass through a skimmer before entering a radiofrequency (RF) hexapole ion guide and RF quadrupole mass filter that direct them into a linear RF octupole ion trap held at 5 K and filled with a buffer gas mixture of 20:80 H₂:He. Collisions with this cold buffer gas mixture result in effective vibrational, rotational, and electronic cooling of the ions, leading to internal temperatures of around 10 K.^{26, 28-30}

The ions are held approximately 40 ms in the trap before being extracted into an orthogonal Wiley-McLaren time-of-flight mass spectrometer³¹ and focused into the interaction region of a standard three-plate Eppink-Parker VMI electrostatic lens assembly.³² In the VMI spectrometer, the ions are photodetached using the frequency-doubled output of a dye laser pumped by the second harmonic of a Nd:YAG laser operating at 20 Hz.

The resulting photoelectrons are projected onto a 2D detector comprising two chevron-stacked microchannel plates coupled to a phosphor screen, which is photographed by a CCD camera after each laser shot.³³ Each image is analyzed for individual electron events for which the centroids are calculated and binned into a 1024 × 1024 grid.³⁴ The three-dimensional electron velocity distribution is reconstructed from the accumulated images using an inverse-Abel method.³⁵ The radial position of features in the reconstructed image is related to electron kinetic energy (eKE) by acquiring VMI images for detachment from atomic F⁻ at several photon energies.³⁶

The VMI spectrometer has an approximately constant resolving power, $\Delta eKE/eKE$,³² yielding the highest eKE resolution for slow photoelectrons. As such, a SEVI spectrum is acquired by first taking an overview spectrum at a sufficiently high photon energy to access all (or most) of the photodetachment transitions before tuning the detachment laser to energies slightly above features of interest. This procedure results in the collection of high-resolution spectra over narrow energy windows that are then concatenated and scaled to match intensities in the overview spectrum, which is less sensitive to variation of the photodetachment cross section with photon energy. Spectra are plotted as a function of electron binding energy (eBE), given by $eBE = hv - eKE$.

III. Computational Methods:

Electronic structure calculations for the $\tilde{X}^2 \Pi_g$ state of NiO_2^- and the $\tilde{X}^1 \Sigma_g^+$ state of NiO_2 were carried out at the coupled-cluster singles doubles augmented with a noniterative triples [CCSD(T)]³⁷ level of theory to determine the equilibrium structures and the harmonic vibrational frequencies of these states and to enable a Franck-Condon (FC) simulation for the electron detachment transitions from the electronic ground state of NiO_2^- to that of NiO_2 . Scalar-relativistic effects have been taken into account using spin-free exact two-component theory in its one-electron variant (SFX2C-1e)^{38,39} together with the aug-cc-pVTZ basis sets⁴⁰⁻⁴² recontracted for SFX2C-1e calculations. Calculations using a hierarchy of CC methods including CCSD,⁴³ CC singles doubles triples (CCSDT),^{44,45} and CC singles doubles triples quadruples (CCSDTQ)^{46,47} have also been performed for the $\tilde{X}^1 \Sigma_g^+$ state of NiO_2 to examine the reliability of the CCSD(T) results, as this state exhibits strong electron-correlation effects.^{17,18} The results of this analysis are outlined in Table S1 of the Supplementary Information (SI). Harmonic frequency calculations are performed by means of numerical differentiation of analytically evaluated gradients using the analytic-gradient techniques for the CC methods and the SFX2C-1e scheme as implemented in the CFOUR program package.⁴⁸⁻⁵⁵ FC simulations presented here employ the double-harmonic approximation using the fcsquared module⁵⁶ of the CFOUR program.

We have also performed SFX2C-1e equation-of-motion coupled-cluster singles doubles (EOM-CCSD)⁵⁷ and EOM-CC singles doubles triples (EOM-CCSDT)^{58,59} calculations to determine the excitation energies of NiO_2 in the anionic equilibrium structure. These are combined with the computed vertical detachment energy for the ground $\tilde{X}^1 \Sigma_g^+$ state of NiO_2 to describe the vertical detachment energies from the ground state of NiO_2^- to these excited states of NiO_2 . Here aug-cc-pVQZ basis sets were used for EOM-CCSD calculations. The triples corrections have been obtained as the differences between EOM-CCSDT and EOM-CCSD results using cc-pVDZ basis sets. All calculations have been performed using the CFOUR program package,^{53,55} except that the EOM-CCSDT calculations of triplet excited states have been carried out using the MRCC program package.⁶⁰⁻⁶²

IV. Results and Discussion:

The cryo-SEVI spectrum of NiO_2^- is presented in Figure 1. Figure 1a shows the lower-eBE region of structure, spanning 24400–28000 cm^{-1} and covering the ground state band of the NiO_2

$\leftarrow \text{NiO}_2^-$ photodetachment transition previously observed.^{10,11} The higher-energy region of the spectra shown in Figure 1b spans 27550 – 32500 cm^{-1} and encompasses detachment transitions to excited electronic states of NiO_2 as will be discussed in Sections IV.A and IV.D. In both figures, a low-resolution overview spectrum (blue) is displayed above high-resolution composite spectra (black) taken at several photon energies.

These spectra represent a significant improvement over previous anion photoelectron spectroscopy studies.^{10,11} The improved resolution afforded by the cryo-SEVI method reveals not only the electronic transitions to the three lowest-lying states of NiO_2 (features A1, C1, D1, respectively) previously observed, but also a manifold of transitions to vibrationally excited states of the neutral species. Peak assignments, electron binding energies (eBEs), as well as shifts from peak A1 are presented in Tables 1-3, while extracted experimental parameters are presented in Table 4.

In the case of the NiO_2 ground state band, assignments of features are facilitated by our SFX2C-1e-CCSD(T)/aug-cc-pVTZ calculations, which allow for FC simulations to be performed for detachment transitions terminating in the $\tilde{X}^1 \Sigma_g^+$ state of NiO_2 . This simulated spectrum facilitates the definitive vibrational assignments in this state and suggests vibrational assignments for the \tilde{a}^1 and \tilde{A}^1 states of NiO_2 . Notably, there are several strong transitions (B1-17) observed in this spectrum that are not reproduced by our simulations. Moreover, these features (B1-B5, for example) are clearly not present in the overview spectrum and retain considerable intensity near detachment threshold. This trend is depicted in Figure 2, in which spectra collected at three photon energies highlight the differing behavior of these features as photodetachment threshold is approached. As discussed in Section IV.C, our assignments for the B peaks all involve odd changes of vibrational quanta in the non-totally symmetric ν_2 bending mode and are hence Franck-Condon forbidden.

Vibrational frequencies were not calculated for the two observed excited states of NiO_2 , though the even spacing of levels and intensity patterns in the cryo-SEVI spectra lend themselves to tentative assignments to different vibrational levels of these two states of NiO_2 (Section IV.D).

IV.A Computational Results

Our coupled-cluster calculations confirm that the electronic ground state of NiO₂ is the $\tilde{X}^1 \Sigma_g^+$ state, while the ground state of NiO₂⁻ is determined as the $\tilde{X}^2 \Pi_g$ state. The valence orbitals of NiO₂ are composed of the Ni 4s and 3d orbitals and the O 2s and 2p orbitals, as shown in Fig. 3. The corresponding orbital compositions are summarized in Table 5. The Ni 3d_{xz} and 3d_{yz} orbitals together with the O 2p_x and 2p_y orbitals form the $1\tau_g$ bonding orbitals and the $2\tau_g$ anti-bonding orbitals. The Ni $3d_{x^2-y^2}$ and 3d_{xy} orbitals do not mix with oxygen valence orbitals and form the non-bonding $1\mathbf{6}_g$ orbitals. The $2\sigma_g^+$ orbitals consist of contributions from the Ni $3d_{z^2}$ orbitals and the O 2s and 2p_z orbitals. The $1\sigma_g^+$ orbitals are mainly composed of the O 2s and 2p_z orbitals with a small contribution from the Ni 4s orbitals. The ground state of NiO₂ takes a closed-shell configuration $(1\sigma_g^+)^2(1\sigma_u^+)^2(2\sigma_g^+)^2(1\delta_g)^4(3\sigma_g^+)^2(2\sigma_u^+)^2(1\tau_u)^4(1\tau_g)^4(2\tau_g)^0$, with the anti-bonding $2\pi_g$ orbitals left unoccupied. Since the $1\sigma_g^+$, $1\sigma_u^+$, $2\sigma_g^+$, $1\mathbf{6}_g$, $3\sigma_g^+$, $1\pi_g$ orbitals are fully occupied for all electronic states discussed here, we will use the occupation numbers for the $3\sigma_g^+$, $2\sigma_u^+$, $1\pi_u$, and $2\pi_g$ orbitals to denote electronic states. In this notation the ground state of NiO₂ is represented as $(3\sigma_g^+)^2(2\sigma_u^+)^2(1\pi_u)^4(2\pi_g)^0$. The ground $\tilde{X}^2 \Pi_g$ state of NiO₂⁻ places the excess electron in the $2\pi_g$ orbital, which is expected to weaken the Ni-O bond.

Although the ground state wave function of NiO₂ is dominated by a closed shell $(3\sigma_g^+)^2(2\sigma_u^+)^2(1\pi_u)^4(2\pi_g)^0$ configuration, this electronic state exhibits strong electron correlation because of the low-lying anti-bonding $2\pi_g$ orbitals. An analysis as detailed in the Supporting Information shows that CCSD(T) calculations provide reasonably accurate structure and frequencies, in spite of the slow convergence of the CC series. The CCSD(T) results perhaps slightly overestimate the vibrational frequency of the bending mode ν_2 and underestimate those

of the antisymmetric stretching and symmetric stretching modes (Π_3 and Π_1). The ground state of NiO_2^- is dominated by the $(3\sigma_g^+)^2(2\pi_u^+)^2(1\pi_u)^4(2\pi_g)^1$ configuration. As discussed in the Supporting Information, the CCSD(T) results are also reasonably accurate for this electronic state.

We have summarized the adiabatic electron affinity, equilibrium structures, and harmonic frequencies computed at the SFX2C-1e-CCSD(T)/aug-cc-pVTZ level of theory in Table 6 and have utilized these parameters in the FC simulations presented in Figure 1. As expected, the

occupation of an anti-bonding $2\pi_g$ orbital in NiO_2^- significantly increases the Ni-O bond length, e.g., the difference between the Ni-O bond lengths in NiO_2 and NiO_2^- computed at the CCSD(T) level amounts to 0.034 Å. The population of this orbital also reduces the asymmetric stretching frequency of NiO_2^- by around 70 cm^{-1} . The large change in the Ni-O bond length leads to a

significant FC progression for the photodetachment transitions from the $\tilde{X}^2 \Pi_g$ state of NiO_2^- to the $\tilde{X}^1 \Sigma_g^+$ of NiO_2 due to the FC activity of the symmetric stretch $\omega_1(\sigma_g)$ mode, which is responsible for the much of the vibrational structure observed in the photoelectron spectrum of NiO_2^- .

Excitation of a $3\sigma_g^+$, $1\pi_u$ or $2\sigma_u$ electron into an anti-bonding $2\pi_g$ orbital gives rise to several low-lying excited states of NiO_2 . The lowest excited state of NiO_2 is a $^3\Pi_g$ state with the leading configuration $(3\sigma_g^+)^1(2\pi_u^+)^2(1\pi_u)^4(2\pi_g)^1$, which resides 0.56 eV above the ground $\tilde{X}^1 \Sigma_g^+$ state. The corresponding singlet $^1\Pi_g$ state lies 0.88 eV above the ground state. Both states can be accessed from the ground $\tilde{X}^2 \Pi_g$ state of NiO_2^- by detaching a $3\sigma_g^+$ electron. Meanwhile, the detachment of a $1\pi_u$ electron or a $2\sigma_u$ electron leads to a manifold of $(3\sigma_g^+)^2(2\pi_u^+)^2(1\pi_u)^3(2\pi_g)^1$ states and a manifold of $(3\sigma_g^+)^2(2\pi_u^+)^1(1\pi_u)^4(2\pi_g)^1$ states lying around 1.1 eV and 2 eV above the

ground state, respectively. These findings are in good agreement with the MRCI calculations of Hübner,²² and are outlined in Table S2. Details about the EOM-CC computations for excitation energies are documented in the Supporting Information.

IV.B. Ground State Franck-Condon Allowed Transitions

Table 1 lists the vibrational assignments of features arising from the $\tilde{X}^1 \Sigma_g^+ \leftarrow \tilde{X}^2 \Pi_g$ transition. These assignments are informed by the results of our FC simulations as well as the previously reported photoelectron spectrum of Ramond *et al.*¹¹ As features A1-13 are largely reproduced in the simulated spectra, they are assigned to Franck-Condon (FC) allowed transitions within the

$\tilde{X}^1 \Sigma_g^+ \leftarrow \tilde{X}^2 \Pi_g$ photodetachment band of NiO₂. FC-allowed transitions include all Δv

transitions in totally symmetric vibrational modes (σ_g for linear species) and even Δv transitions along non-totally symmetric modes.⁶³

Most prominent among these features is A1, here assigned as the 0_0^0 vibrational origin, allowing for the extraction of a refined electron affinity for NiO₂ and providing an order of magnitude improvement in the precision of this measurement of 3.0464(7) eV, compared to 3.043(5) eV in Ref¹¹. The measured EA here is in good agreement with our calculated value of 3.0405 eV.

Beyond the vibrational origin is a wealth of vibrational structure, owing to an extended

progression in the ν_1 symmetric stretch of NiO₂, where there 1_0^1 , 1_0^2 , 1_0^3 , 1_0^4 , and 1_0^5 transitions are observed (A4, A7, A10, A12, A13, respectively). Weak but allowed transitions involving the non-totally symmetric ν_2 bending and ν_3 anti-symmetric stretching modes contribute to the remainder of the A-features in this band, with a short progression in the ν_2 bending coordinate (

2_0^2 and 2_0^4 , corresponding to A2 and A3, respectively), the appearance of the FC-allowed 3_0^2 transition (A9), and several combination bands including A5, A6, and A8 (see Table 1).

From the harmonic progressions along ν_1 and ν_2 and the appearance of the 3_0^2 transition, we

obtain the frequencies of all three vibrational modes of the $\tilde{X}^1 \Sigma_g^+$ state of NiO₂. These values, $\nu_1 = 745(6)$, $\nu_2 = 122(18)$, and $\nu_3 = 978(16)$ cm⁻¹, are in good agreement with those previously reported from photoelectron spectroscopy ($\nu_1 = 745(30)$ cm⁻¹)¹¹ and FTIR studies of NiO₂ in a Ne matrix ($\nu_1 = 749$ and $\nu_3 = 977.5$ cm⁻¹),¹² as well as our calculated values (Table 6) of $\nu_1 = 774$, $\nu_2 = 135$, and $\nu_3 = 985$ cm⁻¹. Further, the observed frequency for the ν_2 bending mode matches well with an observed but unassigned feature in the Ne matrix data at 129.9 cm⁻¹,⁹ suggesting that this peak was from IR excitation of the ν_2 mode.

IV.C. Ground state Franck-Condon Forbidden Transitions

We now consider the assignments to the features in the $\tilde{X}^1 \Sigma_g^+ \leftarrow \tilde{X}^2 \Pi_g$ band that are not reproduced by our FC simulations, peaks B1-B17 (Table 1). The spacing of these features is consistently ~ 120 cm⁻¹ above that of an allowed transition (as is the case for B1-B9, B13, B17) or ~ 240 cm⁻¹ above another ‘‘B’’ feature (as is the case for B9 \rightarrow B11, B10 \rightarrow B12, B12 \rightarrow B14, B13 \rightarrow B15, B14 \rightarrow B16). The similarity of these spacings with that of our measured value for the ν_2 bending frequency (122(18) cm⁻¹) suggests these features arise from transitions terminating in odd quanta of the non-totally symmetric ν_2 mode. We thus assign peaks B1-B17 to transitions of this type to neutral levels with π_u vibrational symmetry.

These transitions are Franck-Condon forbidden but can arise through Herzberg-Teller (HT) coupling to an excited electronic state with the appropriate symmetry.^{29, 64-66} Briefly, two vibronic states, a and b , can mix through HT-coupling provided their electronic and vibrational

symmetries Γ_{elec} and Γ_{vib} , respectively, satisfy⁶³

$$\Gamma_{elec}^a \otimes \Gamma_{vib}^a \otimes \Gamma_{elec}^b \otimes \Gamma_{vib}^b \supset \Gamma_{TS} \quad (1)$$

Here Γ_{TS} is the totally symmetric representation within the molecular point group. This mixing

then creates two new states $|a_0\rangle = c_{1a}|a\rangle + c_{2a}|b\rangle$ and $|b_0\rangle = c_{1b}|a\rangle + c_{2b}|b\rangle$, each an admixture of

the two zero-order vibronic levels. Thus, if detachment to state b is FC-allowed, then detachment to state a_0 becomes allowed, but will display the electronic character of state b .

In the present case, the electronic and vibrational symmetries of the final states in features B1-

B17, Γ_{elec}^a and Γ_{vib}^a , are Σ_g^+ and π_u , respectively. These states can only be observed if they mix

with a state b that is FC-allowed for detachment from the anion, i.e. $\Gamma_{vib}^b = \sigma_g$, thereby requiring

that the excited electronic state HT-coupled to this state be of Π_u symmetry. Our calculations (Table S2) find that such an excited state resides 2.24 eV above the neutral ground state.

The presence of vibronic coupling here is affirmed by the differing behavior of the FC-forbidden and FC-allowed features as the photon energy is changed, as shown in Figure 2. Here, cryo-SEVI spectra are plotted at three photon energies, showing that as the photon energy is lowered and approaches the detachment threshold, the intensity of features A1 and A2 drops precipitously relative to that of B1 and B3. This effect is ascribed to a reduced photodetachment cross section for feature A1 and A3 at low eKE. Such a difference can be related to the relative scaling of the detachment cross sections at low eKE's, given by the Wigner threshold law:⁶⁷

$$\sigma \propto (eKE)^{l+1/2}, \quad (2)$$

where σ is the detachment cross section and l is the angular momentum of the detached electron. Thus, photodetachment is suppressed more strongly at low eKE for detachment of higher l electrons (see inset of Figure 2), to the centrifugal barrier experienced by the departing electron.

For detachment to the $\tilde{X}^1 \Sigma_g^+$ state of NiO₂, selection rules for molecular photodetachment prohibit detachment of $l = 0$ electrons, and p -wave detachment dominates.⁶⁸ Conversely, transitions terminating in odd quanta along the v_2 normal coordinate do so in a neutral level with

contribution from an excited state of Π_u symmetry, for which detachment can proceed *via* $l = 0$ (*s*-wave) transitions.

The disparity in near-threshold cross-section between the “A” and “B” features is a tell-tale sign of HT coupling in cryo-SEVI spectra,^{29, 64-66} as this indicates that “B” features correspond to detachment with lower values of l than the “A” features, reflecting the electronic character of the Π_u electronic state that lends intensity to these transitions. Consequently, spectra for the “B” peaks can be obtained closer to photodetachment threshold, where cryo-SEVI resolution is improved, leading to narrower features as was observed in the cryo-SEVI spectra of the indenyl and nitrate anions.^{66, 69} As such, we are able to refine our determined value for the ν_2 bending mode of NiO₂ from the position of B1 as 120(7) cm⁻¹.

IV.D *Excited state transitions*

Beyond the strongest vibrational transitions in the $\tilde{X}^1 \Sigma_g^+$ manifold reside the strong features C1 and D1. The positions of these features (3.4447(4) and 3.7886(9) eV, respectively) coincide with the previously observed onset of transitions assigned to the $\tilde{a}^1 \Delta_g$ and $\tilde{b}^1 \Sigma_g^+$ states (3.45(2) and 3.82(3) eV, respectively) of NiO₂ based on a molecular orbital picture.¹⁰ Subsequent theoretical work, however, has determined the low-lying states of NiO₂ as the $\tilde{a}^3 \Pi_g$ and $\tilde{A}^1 \Pi_g$ states.²² These assignments agree with our EOM-CC calculations, which find the same state ordering. We thus assign C1 and D1 as the vibrational origins of the $\tilde{a}^3 \Pi_g \leftarrow \tilde{X}^2 \Pi_g$ and $\tilde{A}^1 \Pi_g \leftarrow \tilde{X}^2 \Pi_g$ transitions, with term energies of 0.3982(7) and 0.7422(10) eV, respectively, determined by the shift in peak location from A1. These reported term energies are more precise than those previously reported (0.40(2) and 0.77(3) eV, respectively),¹⁰ and are in good agreement with our computed term energies of 0.56 and 0.88 eV, validating this reassignment.

Numerous weaker features reside beyond peaks C1 and D1 (C2-C8, D2-D6) that report on the vibrational structure of the $\tilde{a}^3 \Pi_g$ and $\tilde{A}^1 \Pi_g$ excited states (Tables 2 and 3). In the $\tilde{a}^3 \Pi_g$ state, there appears to be a progression of a vibrational feature with a frequency of 685(11) cm^{-1} as well as the appearance of the vibrational fundamental and combination bands involving a mode with frequency of 130(5) cm^{-1} . Similarly, in the $\tilde{A}^1 \Pi_g$ state, there appear to be two progressions in features with average spacings of 112(12) and 705(19) cm^{-1} . While we do not have theoretical calculations to make definitive assignments to these features, their relative spacing are close to those of the ν_1 and ν_2 vibrational modes that dominate the structure in the ground state of spectrum NiO_2 . We thus tentatively assign the observed structure to activity along the ν_1 and ν_2 vibrational modes of NiO_2 in the $\tilde{a}^3 \Pi_g$ and $\tilde{A}^1 \Pi_g$ excited states with vibrational frequencies of 685(11) and 130(5) cm^{-1} ($\tilde{a}^3 \Pi_g$) and 705(19) and 112(12) cm^{-1} ($\tilde{A}^1 \Pi_g$), respectively (outlined in Table 4).

Conclusion:

Here, we report high-resolution cryo-SEVI spectra of NiO_2^- showing photodetachment to the $\tilde{X}^1 \Sigma_g^+$, $\tilde{a}^3 \Pi_g$, and $\tilde{A}^1 \Pi_g$ states of NiO_2 . In the ground state, we observe FC-allowed transitions involving the ν_1 symmetric stretch, ν_2 bending, and ν_3 anti-symmetric stretch from which we extract vibrational frequencies of $\nu_1 = 745(6)$, $\nu_2 = 122(18)$, and $\nu_3 = 978(16)$ cm^{-1} , in good agreement with previously reported values. These assignments are facilitated by FC simulations using the SFX2C-1e-CCSD(T)/aug-cc-pVTZ geometries and vibrational frequencies for $\text{NiO}_2^{0/-}$. Notably, we observe extended FC-forbidden progressions to final states with odd quanta in the ν_2 bending coordinate that we ascribe to vibronic coupling to the Π_u excited state of NiO_2 , calculated to reside 2.24 eV above the ground state. From the onset of structure in the ground and excited states, we are able to refine the electron affinity and term energies of NiO_2 and its

first two excited states ($EA = 3.0464(7)$ eV, $T_e(\tilde{a}^3 \Pi_g) = 0.3982(7)$ eV, $T_e(\tilde{A}^1 \Pi_g) = 0.7422(10)$ eV), in good agreement with our calculated values.

Conflicts of interest: There are no conflicts to declare

Acknowledgements: The research conducted at UC Berkeley is funded by the Air Force Office of Scientific Research under Grant No. FA9550-19-1-0051 and the work done at Johns Hopkins University is supported by Department of Energy Early Career Research Program under Award Number DE-SC0020317. M.C.B. thanks the Army Research Office for a National Defense Science and Engineering Graduate fellowship. J.A.L thanks the Alexander von Humboldt Foundation for a Feodor Lynen Research Fellowship.

References:

1. N. A. K. Aramouni, J. G. Touma, B. Abu Tarboush, J. Zeaiter and M. N. Ahmad, *Renew Sust Energy Rev*, 2018, **82**, 2570-2585.
2. C. Alvarez-Galvan, M. Melian, L. Ruiz-Matas, J. L. Eslava, R. M. Navarro, M. Ahmadi, B. Roldan Cuenya and J. L. G. Fierro, *Front Chem*, 2019, **7**.
3. E. Heracleous, A. F. Lee, K. Wilson and A. A. Lemonidou, *J Catal*, 2005, **231**, 159-171.
4. Y. L. Zhou, F. F. Wei, J. Lin, L. Li, X. Y. Li, H. F. Qi, X. L. Pan, X. Y. Liu, C. D. Huang, S. Lin and X. D. Wang, *ACS Catal.*, 2020, **10**, 7619-7629.
5. S. Dey, G. C. Dhal, D. Mohan and R. Prasad, *Adv Compos Hybrid Ma*, 2019, **2**, 626-656.
6. A. W. Castleman, *Catal Lett*, 2011, **141**, 1243-1253.
7. J. L. Mason, C. N. Folluo and C. C. Jarrold, *J. Chem. Phys.*, 2021, **154**.
8. H. Huber and G. A. Ozin, *Can J Chemistry*, 1972, **50**, 3746-&.
9. A. Citra, G. V. Chertihin, L. Andrews and M. Neurock, *J Phys Chem A*, 1997, **101**, 3109-3118.
10. H. B. Wu and L. S. Wang, *J Chem Phys*, 1997, **107**, 16-21.
11. T. M. Ramond, G. E. Davico, F. Hellberg, F. Svedberg, P. Salen, P. Soderqvist and W. C. Lineberger, *J Mol Spectrosc*, 2002, **216**, 1-14.
12. F. Allouti, L. Manceron and M. E. Alikhani, *Phys Chem Chem Phys*, 2006, **8**, 448-455.
13. W. D. Vann, R. L. Wagner and A. W. Castleman, *J Phys Chem A*, 1998, **102**, 1708-1718.
14. M. C. Oliveira, J. Marcalo, M. C. Vieira and M. A. A. Ferreira, *Int J Mass Spectrom*, 1999, **185**, 825-835.
15. J. U. Reveles, G. E. Johnson, S. N. Khanna and A. W. Castleman, *J Phys Chem C*, 2010, **114**, 5438-5446.
16. C. Salvitti, M. Rosi, F. Pepi, A. Troiani and G. de Petris, *Chem Phys Lett*, 2021, **776**.
17. M. R. A. Blomberg, E. M. Siegbahn and A. Strich, *Chem Phys*, 1985, **97**, 287-301.
18. C. W. Bauschlicher, *J Phys Chem A*, 2004, **108**, 2871-2873.
19. K. Deng, J. L. Yang and Q. S. Zhu, *J Chem Phys*, 2003, **118**, 6868-6873.
20. G. L. Gutsev, B. K. Rao and P. Jena, *The Journal of Physical Chemistry A*, 2000, **104**, 11961-11971.
21. E. L. Uzunova, H. Mikosch and G. S. Nikolov, *J Chem Phys*, 2008, **128**.
22. O. Hubner and H. J. Himmel, *J Phys Chem A*, 2012, **116**, 9181-9188.
23. D. M. Neumark, *J Phys Chem A*, 2008, **112**, 13287-13301.
24. M. L. Weichman and D. M. Neumark, *Annu Rev Phys Chem*, 2018, **69**, 101-124.
25. A. Osterwalder, M. J. Nee, J. Zhou and D. M. Neumark, *J Chem Phys*, 2004, **121**, 6317-6322.
26. C. Hock, J. B. Kim, M. L. Weichman, T. I. Yacovitch and D. M. Neumark, *J Chem Phys*, 2012, **137**.
27. U. Even, J. Jortner, D. Noy, N. Lavie and C. Cossart-Magos, *J Chem Phys*, 2000, **112**, 8068-8071.
28. J. B. Kim, C. Hock, T. I. Yacovitch and D. M. Neumark, *J Phys Chem A*, 2013, **117**, 8126-8131.

29. J. A. DeVine, M. L. Weichman, B. Laws, J. Chang, M. C. Babin, G. Balerdi, C. J. Xie, C. L. Malbon, W. C. Lineberger, D. R. Yarkony, R. W. Field, S. T. Gibson, J. Y. Ma, H. Guo and D. M. Neumark, *Science*, 2017, **358**, 336-339.
 30. M. C. Babin, J. A. DeVine, M. L. Weichman and D. M. Neumark, *J Chem Phys*, 2018, **149**.
 31. W. C. Wiley and I. H. McLaren, *Rev Sci Instrum*, 1955, **26**, 1150-1157.
 32. A. T. J. B. Eppink and D. H. Parker, *Rev Sci Instrum*, 1997, **68**, 3477-3484.
 33. D. W. Chandler and P. L. Houston, *J Chem Phys*, 1987, **87**, 1445-1447.
 34. M. B. Doyle, C. Abeyasera and A. G. Suits, *Journal*, 2017.
 35. E. W. Hansen and P. L. Law, *J Opt Soc Am A*, 1985, **2**, 510-520.
 36. C. Blondel, C. Delsart and F. Goldfarb, *J Phys B-at Mol Opt*, 2001, **34**, L281-L288.
 37. K. Raghavachari, G. W. Trucks, J. A. Pople and M. Head-Gordon, *Chem Phys Lett*, 1989, **157**, 479-483.
 38. K. G. Dyall, *J Chem Phys*, 2001, **115**, 9136-9143.
 39. W. J. Liu and D. L. Peng, *J Chem Phys*, 2009, **131**.
 40. T. H. Dunning, *J Chem Phys*, 1989, **90**, 1007-1023.
 41. R. A. Kendall, T. H. Dunning and R. J. Harrison, *J Chem Phys*, 1992, **96**, 6796-6806.
 42. N. B. Balabanov and K. A. Peterson, *J Chem Phys*, 2005, **123**.
 43. G. D. Purvis and R. J. Bartlett, *J Chem Phys*, 1982, **76**, 1910-1918.
 44. J. Noga and R. J. Bartlett, *J Chem Phys*, 1987, **86**, 7041-7050.
 45. G. E. Scuseria and H. F. Schaefer, *Chem Phys Lett*, 1988, **152**, 382-386.
 46. S. A. Kucharski and R. J. Bartlett, *Theor Chim Acta*, 1991, **80**, 387-405.
 47. N. Oliphant and L. Adamowicz, *J Chem Phys*, 1991, **95**, 6645-6651.
 48. J. Gauss, J. F. Stanton and R. J. Bartlett, *J Chem Phys*, 1991, **95**, 2623-2638.
 49. J. F. Stanton, J. Gauss, J. D. Watts and R. J. Bartlett, *J Chem Phys*, 1991, **94**, 4334-4345.
 50. J. D. Watts, J. Gauss and R. J. Bartlett, *Chem Phys Lett*, 1992, **200**, 1-7.
 51. L. Cheng and J. Gauss, *J Chem Phys*, 2011, **135**.
 52. D. A. Matthews and J. F. Stanton, *J Chem Phys*, 2015, **142**.
 53. D. A. Matthews, L. Cheng, M. E. Harding, F. Lipparini, S. Stopkowicz, T. C. Jagau, P. G. Szalay, J. Gauss and J. F. Stanton, *J Chem Phys*, 2020, **152**.
 54. D. A. Matthews, *J Chem Theory Comput*, 2020, **16**, 6195-6206.
 55. J. G. J.F. Stanton, L. Cheng, M.E. Harding, D.A. Matthews, P.G. Szalay, CFOUR, coupled-cluster techniques for computational chemistry, a quantum-chemical program package, with contributions from
A.A. Auer, R.J. Bartlett, U. Benedikt, C. Berger, D.E. Bernholdt, S. Blaschke, Y.J. Bomble, S. Burger, O. Christiansen, D. Datta, F. Engel, R. Faber, J. Greiner, M. Heckert, O. Heun, M. Hilgenberg, C. Huber, T.-C. Jagau, D. Jonsson, J. Jusélius, T. Kirsch, K. Klein, G.M. Kopper, W.J. Lauderdale, F. Lipparini, T. Metzroth, L.A. Mück, T. Nottoli, D.P. O'Neill, D.R. Price, E. Prochnow, C. Puzzarini, K. Ruud, F. Schiffmann, W. Schwalbach, C. Simmons, S. Stopkowicz, A. Tajti, J. Vázquez, F. Wang, J.D. Watts and the integral packages
- MOLECULE (J. Almlöf and P.R. Taylor), PROPS (P.R. Taylor), ABACUS (T. Helgaker, H.J. Aa. Jensen, P. Jørgensen, and J. Olsen), and ECP routines by A. V. Mitin and C. van Wüllen, For the current version, see <http://www.cfour.de>.
56. S. M. Rabidoux, V. Eijkhout and J. F. Stanton, *J Chem Theory Comput*, 2016, **12**, 728-739.

57. J. F. Stanton and R. J. Bartlett, *J Chem Phys*, 1993, **98**, 7029-7039.
58. K. Kowalski and P. Piecuch, *J Chem Phys*, 2001, **115**, 643-651.
59. S. A. Kucharski, M. Wloch, M. Musial and R. J. Bartlett, *J Chem Phys*, 2001, **115**, 8263-8266.
60. M. Kallay and P. R. Surjan, *J Chem Phys*, 2001, **115**, 2945-2954.
61. M. Kallay and J. Gauss, *J Chem Phys*, 2004, **121**, 9257-9269.
62. M. Kallay, P. R. Nagy, D. Mester, Z. Rolik, G. Samu, J. Csontos, J. Csoka, P. B. Szabo, L. Gyevi-Nagy, B. Hegely, I. Ladjanszki, L. Szegedy, B. Ladoczki, K. Petrov, M. Farkas, P. D. Mezei and A. Ganyecz, *J Chem Phys*, 2020, **152**.
63. G. Herzberg, *Electronic spectra and electronic structure of polyatomic molecules*, Van Nostrand Reinhold Company, Princeton, NJ, 1966.
64. J. A. DeVine, A. Abou Taka, M. C. Babin, M. L. Weichman, H. P. Hratchian and D. M. Neumark, *J Chem Phys*, 2018, **148**.
65. M. L. Weichman, L. Cheng, J. B. Kim, J. F. Stanton and D. M. Neumark, *J Chem Phys*, 2017, **146**.
66. M. C. Babin, J. A. DeVine, M. DeWitt, J. F. Stanton and D. M. Neumark, *J Phys Chem Lett*, 2020, **11**, 395-400.
67. E. P. Wigner, *Phys Rev*, 1948, **73**, 1002-1009.
68. K. J. Reed, A. H. Zimmerman, H. C. Andersen and J. I. Brauman, *J Chem Phys*, 1976, **64**, 1368-1375.
69. J. B. Kim, M. L. Weichman, T. I. Yacovitch, C. Shih and D. M. Neumark, *J Chem Phys*, 2013, **139**.

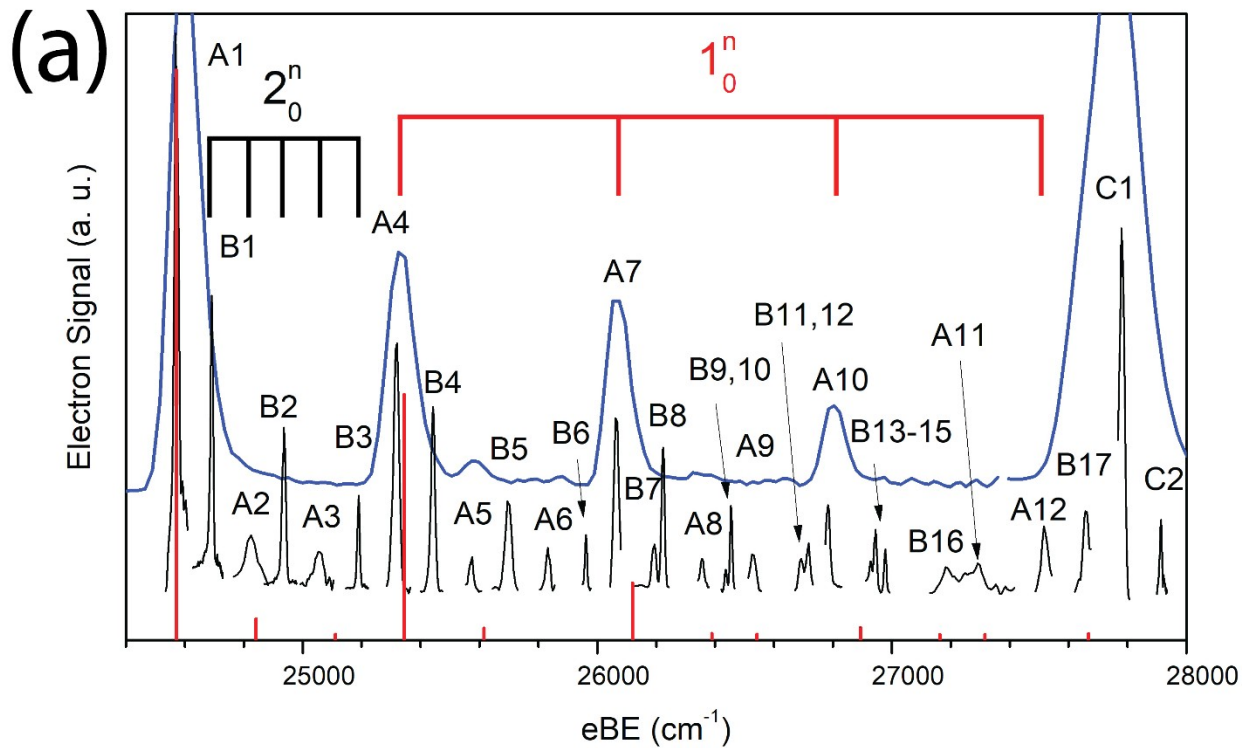


Figure 1. Cryo-SEVI spectra of NiO_2^- showing detachment to the (a) $\tilde{X}^1 \Sigma_g^+$ ground state and (b) $\tilde{a}^1 \Delta_g$ and $\tilde{A}^1 \Pi_g$ excited states. Blue traces are low-resolution overview scans taken with photon energies of 30394 and 35025 cm^{-1} for panels (a) and (b), respectively. Black traces are high-resolution scans taken at variable photon energies, while red stick spectra in (a) represent FC simulations for the $\tilde{X}^1 \Sigma_g^+ \leftarrow \tilde{X}^2 \Pi_g$ photodetachment transition from NiO_2^- . Vibrational modes for the ground state are depicted below the ground-state spectrum.

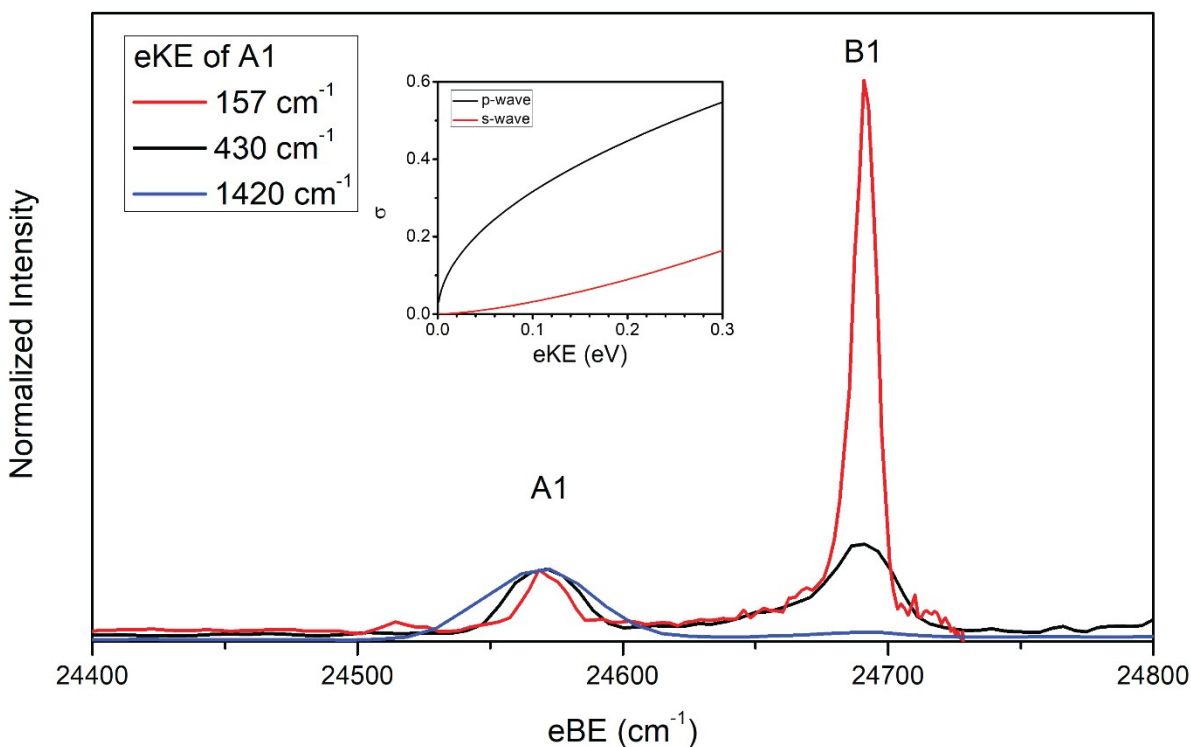


Figure 2. Cryo-SEVI spectra of NiO_2^- at three photon energies illustrating the differing signal attenuation for features A1 and B1 as eKE decreases. The intensity of each scan has been normalized to feature A1. Photon energies employed are 25991 (blue), 25001 (black), and 24728 cm^{-1} (red). Insert: photodetachment cross-section as a function of kinetic energy for s - and p -wave detachment as outlined by the Wigner threshold law.⁶⁷

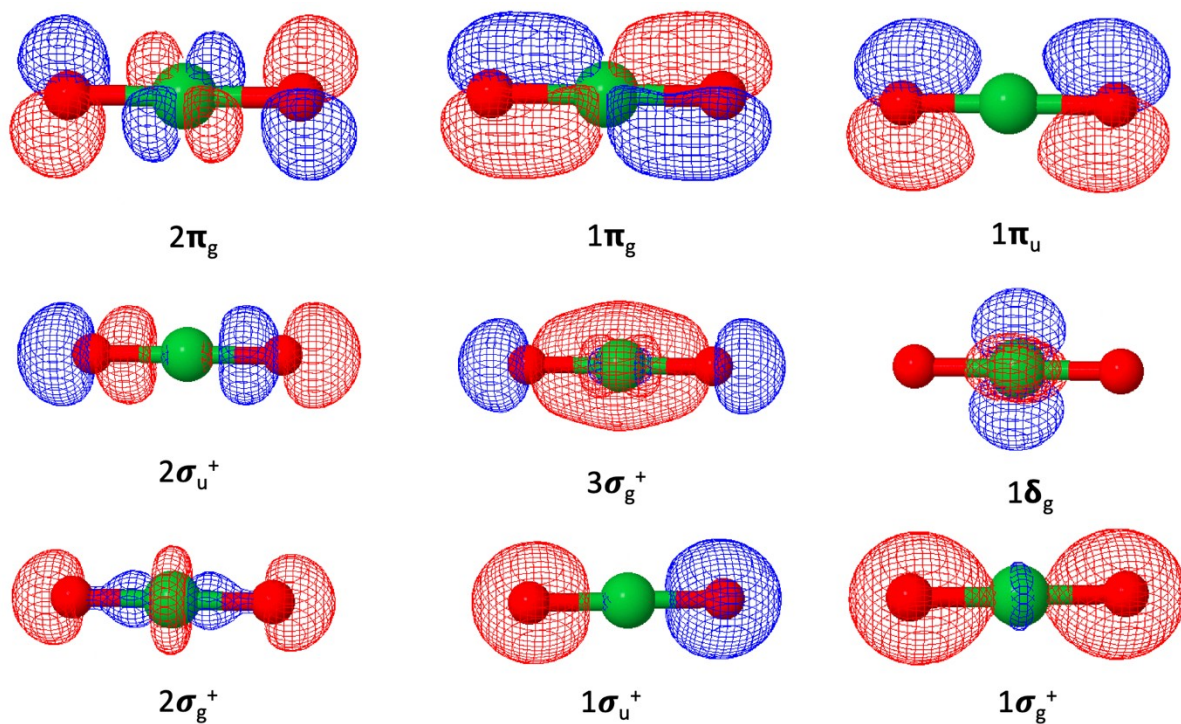


Figure 3. Valence molecular orbitals of NiO₂ originating from the Ni 4*s* and 3*d* orbitals and the O 2*s* and 2*p* orbitals.

Table 1. Peak positions, shifts from peak A1, and assignments, in units of cm^{-1} , for the

$\tilde{X}^1 \Sigma_g^+ \leftarrow \tilde{X}^2 \Pi_g$ detachment transitions of NiO_2^- . Uncertainty in the peak positions correspond to one standard deviation from a Gaussian fit to the highest-resolution experimental trace for each feature.

Peak	eBE	Shift	Assignment
A1	24571(6)	-	0_0^0
B1	24691(7)	120	2_0^1
A2	24815(13)	244	2_0^2
B2	24936(8)	365	2_0^3
A3	25061(12)	490	2_0^4
B3	25190(7)	619	2_0^5
A4	25316(6)	745	1_0^1
B4	25442(9)	871	$1_0^1 2_0^1$
A5	25572(9)	1001	$1_0^1 2_0^2$
B5	25700(8)	1129	$1_0^1 2_0^3$
A6	25832(9)	1261	$1_0^1 2_0^4$
B6	25961(7)	1390	$1_0^1 2_0^5$
A7	26065(8)	1494	1_0^2
B7	26192(9)	1621	$1_0^1 2_0^7$
B8	26223(7)	1652	$1_0^2 2_0^1$
A8	26356(9)	1786	$1_0^2 2_0^2$
B9	26436(6)	1865	$1_0^1 2_0^9$
B10	26454(7)	1883	$1_0^2 2_0^3$
A9	26529(11)	1957	3_0^2
B11	26692(9)	2121	$2_0^1 3_0^2$
B12	26716(9)	2145	$1_0^2 2_0^5$
A10	26783(9)	2212	1_0^3
B13	26928(10)	2357	2_0^1
B14	26945(7)	2374	$1_0^2 2_0^7$

B15	26978(7)	2406	$1_0^3 2_0^3$
B16	27187(28)	2616	$1_0^2 2_0^9$
A11	27283(35)	2712	$1_0^1 3_0^2$
A12	27519(11)	2948	1_0^4
B17	27660(11)	3089	$1_0^4 2_0^1$
A13	28260(11)	3689	1_0^5

Table 2. Peak positions, shifts from peak A1, and assignments, in units of cm^{-1} , for the

$\tilde{a}^3 \Pi_g \leftarrow \tilde{X}^2 \Pi_g$ detachment transitions of NiO_2^- . Uncertainty in the peak positions correspond to one standard deviation from a Gaussian fit to the highest-resolution experimental trace for each feature.

Peak	eBE	Shift	Assignment
C1	27783(3)	-	$\tilde{a}^3 \Pi_g 0_0^0$
C2	27913(5)	131	2_0^1
C3	28468(11)	685	1_0^1
C4	28589(13)	807	$1_0^1 2_0^1$
C5	29162(12)	1380	1_0^2
C6	29271(17)	1488	$1_0^2 2_0^1$
C7	29883(9)	2100	1_0^3
C8	29968(15)	2186	$1_0^3 2_0^1$

Table 3. Peak positions, shifts from peak A1, and assignments, in units of cm^{-1} , for the

$\tilde{A}^1 \Pi_g \leftarrow \tilde{X}^2 \Pi_g$ detachment transitions of NiO_2^- . Uncertainty in the peak positions correspond to one standard deviation from a Gaussian fit to the highest-resolution experimental trace for each feature.

Peak	eBE	Shift	Assignmen
			t
D1	30557(7) 30669(12)	-	$\tilde{A}^1 \Pi_g 0_0^0$
D2) 30814(10)	112	2_0^1
D3) 31263(19)	257	2_0^2
D4) 31422(16)	706	1_0^1
D5)	865	$1_0^1 2_0^1$

D6	31944(9)	1275	1_0^+
----	----------	------	---------

Table 4. Experimental parameters for the various states of NiO₂ probed in this work, extracted from the cryo-SEVI spectra of photodetachment of NiO₂⁻, along with comparison to our SFX2C-1e-CCSD(T)/aug-cc-pVTZ theoretical calculations for the ground state and EOM-CCSDT/cc-pVDZ calculations for the excited state term energies. Available literature values are presented.

	Parameter	Calculate		
		d	SEVI	Literature
$\tilde{X}^1 \Sigma_g^+$	EA (eV)		3.0464(7)	3.043(5) ^a
	ω_1 (cm ⁻¹)	774	745(6)	749 ^b
	ω_2 (cm ⁻¹)	135	120(7)	
	ω_3 (cm ⁻¹)	985	978(16)	977.5 ^b
$\tilde{a}^3 \Pi_g$	T _e (eV)	0.56	0.3982(7)	0.40(2) ^c
	ω_1 (cm ⁻¹)		685(11)	
	ω_2 (cm ⁻¹)		131(5)	
$\tilde{A}^1 \Pi_g$			0.7422(10)	
	T _e (eV)	0.88)	0.77(3) ^c
	ω_1 (cm ⁻¹)		706(19)	
	ω_2 (cm ⁻¹)		112(12)	

^a = Ref ¹¹ ^b = Ref ¹² ^c = Ref ¹⁰

Table 5. The principal compositions of valence molecular orbitals of NiO₂. Significant secondary contributions are enclosed in the brackets.

Molecular orbitals	Compositions
1 σ_g^+	O 2s
1 σ_u^+	O 2s
2 σ_g^+	Ni 3d _{z²} [O 2s and 2p _z]
1 δ_g	Ni 3d _{x²-y²} and 3d _{xy}
3 σ_g^+	O 2s, 2p _z [Ni 4s, 3d ₀]
2 σ_u^+	O 2s, 2p _z
1 π_u	O 2p _x and 2p _y
1 π_g	O 2p _x and 2p _y [Ni 3d _{xz} and 3d _{yz}]
2 π_g	Ni 3d _{xz} and 3d _{yz} [O 2p _x and 2p _y]

Table 6. Computed adiabatic electron affinity (EA_a), bond lengths, and harmonic vibrational

frequencies for the X¹Σ_g⁺ state of NiO₂ and the $\tilde{X}^2\Pi_g$ state of NiO₂⁻. Scalar-relativistic effects have been taken into account using the SFX2C-1e scheme. The aug-cc-pVTZ basis sets recontracted for the SFX2C-1e scheme have been used. Reported values are in cm⁻¹ except for bond length, which is reported in Å.

	R(Ni-O)	$\omega_1(\sigma_g)$	$\omega_2(\tau_u)$	$\omega_3(\sigma_u)$	EA _a
NiO ₂	1.609	774	135	985	24523
NiO ₂ ⁻	1.643	772	96	915	--